# Thermal emission of holes from defects in uniaxially stressed *p*-type silicon

D. D. Nolte*
*Center for Advanced Materials, Lawrence Berkeley Laboratory, University of California at Berkeley, Berkeley, California 94720*

E. E. Haller
*Center for Advanced Materials, Lawrence Berkeley Laboratory, University of California at Berkeley, Berkeley, California 94720 and Department of Materials Science and Mineral Engineering, University of California at Berkeley, Berkeley, California 94720*

(Received 23 May 1988)

Iron-acceptor pair defects in silicon are insensitive to stress. These defects therefore provide convenient reference points from which to measure the effects of uniaxial stress on the valence-band structure in silicon. Despite the strong mixing of light- and heavy-hole bands at low values of stress, we find that for thermal emission the stress-split valence band can be approximated as two independent bands that displace rigidly with increasing stress according to the shear deformation potentials. The spherical approximation for the effective masses is not consistent with these deformation potentials because the approximation incorrectly partitions the density of states between the two bands. We establish the correct partitioning of the density of states numerically, and find stress-dependent density of states that approximately conserve the center of gravity of the split valence bands. Uniaxial stress data on the Fe-Al defects in silicon are used to experimentally verify the numerical results. The analysis described in this paper can be easily generalized to determine the stress properties of hole traps in any *p*-type semiconductor.

## I. INTRODUCTION

Semiconductors are placed in states of uniaxial stress for many different applications. Far-infrared detectors based on shallow-level absorption are often placed under uniaxial stress to extend the sensitivity of the detectors to longer wavelengths.[1] Carrier statistics, and particularly the density of states at the band edge, play an important role in these devices by defining defect occupancies and carrier detrapping lifetimes. Uniaxial stress is also commonly used as a probe of defect symmetry and structure. There has been recent work in the use of uniaxial stress in conjunction with thermally stimulated emission of carriers from deep-level defects.[2,3] This thermal ionization technique is also known as deep-level transient spectroscopy (DLTS).[4–7] Defect energies are derived by measuring the rates of thermal emission of carriers from defects to the band edge. The emission probability is defined through detailed balance, which includes the density of states in the band and the thermal velocities of the carriers. For these applications and techniques, it is crucial to understand how the uniaxial stress affects the thermal emission of carriers from defects to a stress-split valence band.

There have been decades of research covering the stress properties of the valence-band edges (and shallow acceptors) in semiconductors. Much of the theoretical[8,9] and experimental work[10] has been focused on defining the effective masses and the deformation potentials of the band extrema. The typical analysis techniques include excitonic recombination luminescence[11,12] and cyclotron resonance,[13] all studied successfully under uniaxial stress. The structure of the valence band has presented a challenge because of its nonparabolic energy bands. The valence band in silicon is also complicated by the small spin-orbit splitting. The energy splittings of the valence-band edge have been measured accurately using luminescence, and are found to vary nonlinearly with stress because of interaction with the split-off band. The curvature of the valence band has been studied through cyclotron resonance under uniaxial stress. Good agreement has been found between theory and experiment for large stresses.[8,14]

These analysis techniques investigate the stress properties of the band extrema alone; they do not give a good measure of the effects on the energy band structure at wave vectors away from the extremum point in **k** space. Yet the thermal properties of carriers in the bands at finite temperatures depend strongly on the band structure away from the extremum. In this paper we emphasize the thermal emission probability of holes from electrically active defects in the band gap to the valence-band edge. It therefore must be considered how stress affects valence-band states with energies several $k_B T$ from the band edge. The results derived for the band-edge effective density of states and the thermal velocities are general and can be used for any problem involving carrier statistics under stress. This paper begins by describing the stress insensitivity of the iron-acceptor pairs in silicon, justifying their use as reference points for measuring the effects of uniaxial stress on the valence band. The zero-stress structure of the valence band is described briefly, including the difficulty of defining an effective mass. In Sec. IV we present the derivation of thermal emission from defects to multiple, parabolic bands and generalize the results to include the continuous energy

 

dispersion of a band with a complicated structure such as the valence band under uniaxial stress. The effects of stress on the thermal emission of holes from defects to the valence band is discussed in depth in Sec. V. We develop an independent-band model that describes the valence band as two parabolic bands that displace rigidly with increasing stress according to the deformation potentials $b$ and $d$. For this choice of the energy shifts, the effective masses describing the density of states must be chosen consistently. The spherical approximation is not consistent with these deformation potentials because the approximation incorrectly partitions the density of states between the two bands. We establish the correct partitioning of the density of states through numerical integration of the Bir-Pikus Hamiltonian, and find stress-dependent effective masses that approximately conserve the center of gravity of the split valence bands. Experimental verification of the independent-band model using the effective masses derived in Sec. V is provided in Sec. VI with the presentation of uniaxial-stress deep-level transient spectroscopy (DLTS) data on Fe-Al pairs in silicon.

## II. IRON-ACCEPTOR DEFECTS IN SILICON

Iron-acceptor pairs are the dominant deep-level defects present in $p$-type silicon following iron diffusion and quenching. These defects include the species Fe-B, Fe-Al, Fe-Ga, and Fe-In. The pairing reaction occurs in $p$-type material in which the Fermi energy lies in the lower half of the gap. For this position of the Fermi level, both the iron and the acceptor are ionized, but with opposite charge. The resulting Coulomb attraction between the ionized donor and acceptor provides the mechanism for the capture of the mobile interstitial iron by the substitutional group III element.

Iron-acceptor pairs in silicon were first detected by Ludwig and Woodbury[15] using electron paramagnetic resonance (EPR). The defects were found to be highly anisotropic and to exhibit trigonal symmetry, except for FeIn which exhibited orthorhombic symmetry (ordinarily called rhombic $I$). Recently a rhombic $I$ configuration has also been identified[16] for Fe-Al using EPR. Detailed studies of the EPR of Fe-B pairs in silicon have been carried out independently by Gehlhof and Segsa[17] and van Kooten, Weller, and Ammerlan.[16] They both arrive at a strong negative trigonal field. On physical grounds the trigonal field would be expected to be strongly repulsive because of the negative charge of the boron. The model for the iron-acceptor pairs (derived from the EPR data) places the iron in the tetrahedral interstitial site adjacent to the substitutional boring in the trigonal centers (2.35-Å nearest-neighbor separation). In the rhombic $I$ center of Fe-Al the iron is assumed to be situated in the next-nearest-neighbor interstitial site with respect to the boron (2.72-Å next-nearest-neighbor separation). Of course, the iron atom is likely to relax towards the substitutional site because of the attractive Coulomb field.

Iron-acceptor pairs in silicon have been studied extensively using deep-level transient spectroscopy.[18,19] After iron diffusion in silicon a level is observed at $E_v + 0.44$ eV. This level is assigned to the isolated interstitial iron. A level is also observed at $E_v + 0.10$ eV in Si:B after iron diffusion which has been ascribed to the Fe-B pair. Two defect levels have been observed in Si:Al after iron diffusion, one at $E_v + 0.13$ eV and another at $E_v + 0.20$ eV. These are designated as Fe-Al-2 and Fe-Al-1, respectively, and have tentatively been identified as the rhombic $I$ and trigonal Fe-Al configurations observed in EPR.

The most interesting feature of the iron-acceptor pairs is their metastability. Chantre and Bois have demonstrated[20] that the Fe-Al-2 defect is a metastable state of the Fe-Al-1 defect. The transformation between the two configurations is controlled by charge-state dependencies of the total energy. The activation energy for the transformation is about 0.5 eV. The phenomenological model proposed to explain this metastability is based on the electrostatic energy of the $Fe^+$ in the electric field of the ionized acceptor. The iron atom in the stable state is assumed to lie in the nearest-neighbor interstitial site, while in the metastable state it is assumed to lie in the next-nearest-neighbor interstitial site (this model is identical to the model proposed to explain the EPR results of Fe-Al). This model gives reasonable predictions for the energy differences between the stable and metastable states, and the activation energy for transformation is of the same order as the activation energy for diffusion of interstitial iron.

### A. Insensitivity to stress

The paramagnetic iron-acceptor center is attributed to the $3d^7$ configuration of the iron. The hyperfine splitting from the interaction with the spin $\frac{3}{2}$ on $^{11}B$ is clearly observable and gives an unambiguous identification of the defect. The Fe-B as well as one of the Fe-Al EPR signals show strongly anisotropic $g$ tensors with $C_{3v}$ symmetry. This symmetry is consistent with the iron occupying the nearest interstitial site adjacent to the ionized acceptor. Recently, uniaxial stress was applied in conjunction with EPR to attempt to observe electronic redistribution or reorientation of the $C_{3v}$ axis of Fe-B pairs.[21] No significant changes in the amplitudes of the EPR signals originating from the defects parallel and off parallel to the stress direction were observed. From the magnitude of the stress and the temperature at which the stress was applied, an upper limit of 0.3 eV per unit strain was set for the strain coupling of the defect. From this upper limit, we can conclude that the Fe-B pairs will show energy splittings from uniaxial stress less than 3 meV/GPa. This value is consistent with predicted magnitudes of the shear deformation potentials for these defects[22] based on the electrostatic model of Chantre and Bois. Such small splittings are below the resolution of DLTS. Contributions to the stress dependence of the iron-acceptor pairs from remnant orbital degeneracy (or near degeneracy) is still possible, and these effects could produce anisotropic energy shifts (although no splittings), but the magnitudes of the anisotropy[23] are still likely to be only the order of 5 meV/GPa.

The hydrostatic shifts of the Fe-Al pairs have been measured under hydrostatic pressure[24,25] to be 12 meV/GPa for Fe-Al-1 and 9.6 meV/GPa for Fe-Al-2.

Uniaxial stress has a hydrostatic component equal to one-third that of hydrostatic stress. A small shift of roughly $-3$ meV/GPa towards the valence band will occur for the defect energy from the hydrostatic component of the uniaxial stress. This value, as well as the possible shear anisotropy of less then 5 meV/GPa, are both much smaller than the energy shift of between 20 and 30 meV/GPa that the top of the valence band experiences under uniaxial stress. Therefore the iron-acceptor pairs are relatively insensitive to stress and we can use the stress dependence of the DLTS spectrum of iron-acceptor pairs as a probe of the effects of stress on the valence band.

### B. Stressed DLTS data

Iron was diffused for 2 h at 1000 °C into $(1\times6\times10)$-mm$^3$ oriented samples of $5\times10^{15}$ cm$^{-3}$ aluminum- or boron-doped silicon. The samples were quenched in air. The quench is necessary to capture the iron as interstitials without precipitation. The samples were etched and allowed to oxidize before evaporation of the contacts. We evaporated 300 Å of gold onto one surface to form the Ohmic contact. The rectifying contact was formed by evaporating 1000 Å of Al onto the opposite side. The evaporation was performed with minimal current in order to avoid heating of the contact. The aluminum was covered by 300 Å of gold to protect the aluminum from the indium electrical contacts. Typical concentrations of the Fe-Al levels after preparation ranged from $5\times10^{12}$ to $5\times10^{13}$ cm$^{-3}$.

The stress samples were cut from the contacted sample into $(1\times1\times6)$-mm$^3$ parallelepipeds. The ends of the cut samples were etched to remove the sharp edges. We attached 32-gauge wire to the samples using pressed indium contacts. Samples were mounted into a DLTS stress apparatus capable of achieving 1 GPa of uniaxial stress on a sample with a 1-mm$^2$ cross section. The stress data were taken with the time constant of the DLTS correlator set to a fixed value, around 3 ms. Zero-stress data were taken and then the stress was increased by intervals of about 0.1 GPa to nearly 1 GPa. The zero-stress measurement was repeated afterwards to check for stress hysteresis. Data were always taken for increasing temperature under 0.01 atm of helium exchange gas in order to equilibrate the temperatures within the stress rig and remove any effects from thermal hysteresis. Characteristic DLTS data for iron-boron pairs in silicon are shown in Fig. 1 for [110]-oriented stress. The DLTS peak experiences a dramatic shift to lower temperature with increasing stress. Furthermore, the shift appears to be nonlinear, with asymptotic behavior at low stress. In view of the stress insensitivity of the iron-boron pairs, these two features arise predominantly from the effects of stress on the valence band. The goal of this paper is to understand, in detail, all the contributions to the temperature shift of thermal emission from hole traps in uniaxially stressed $p$-type material.

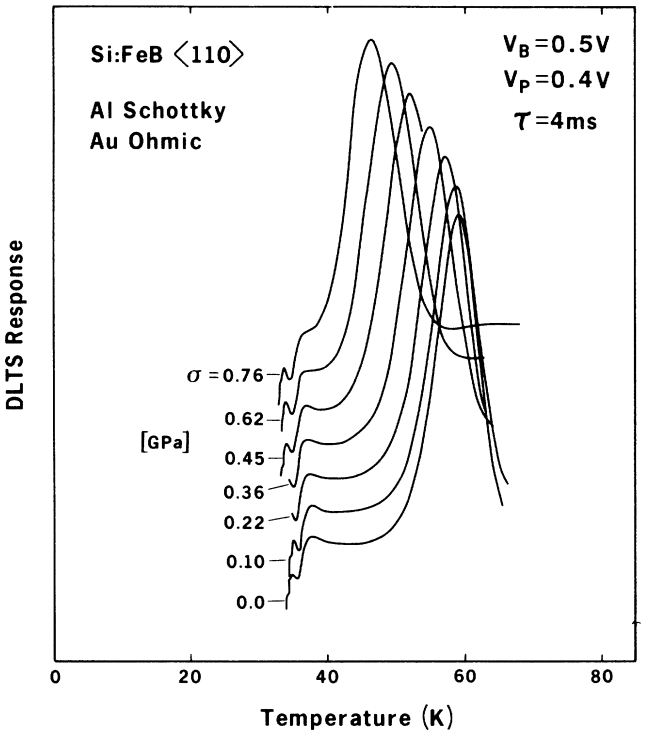


FIG. 1. Shift of the DLTS peak as a function of increasing [110]-oriented uniaxial stress for Fe-B in silicon.

## III. STRUCTURE OF THE VALENCE BAND

The top of the valence band in silicon originates from the three valence $p$ orbitals of silicon. At the center of the Brillouin zone the band is threefold degenerate (in the absence of spin-orbit effect) and transforms as the $\Gamma_5(O_h)$ representation of the point group of the crystal. For finite $\mathbf{k}$ vector this degeneracy is broken, resulting in energy dispersion with a small and a large curvature. Under the influence of the spin-orbit interaction, the $\Gamma_5$ symmetry at the $\Gamma$ point is broken into a $\Gamma_8$ quartet corresponding to $j=\frac{3}{2}$ and a $\Gamma_7$ doublet corresponding to $j=\frac{1}{2}$, which is split off from the $\Gamma_8$ energy by an amount $\Delta_{\text{s.o.}}$, called the spin-orbit splitting. Silicon is special among the common semiconductors in that the spin-orbit splitting is relatively small compared to the bandgap, $\Delta_{\text{s.o.}}=0.044$ eV compared to $E_{\text{gap}}=1.15$ eV. This small splitting has important consequences for the structure of shallow-acceptor wave functions, and plays a significant role in high-stress experiments.

The energy dispersion, including the spin-orbit interaction, is shown for finite $\mathbf{k}$ vector in Fig. 2. The structure of the valence band is composed of a heavy-hole band and a light-hole band (which are degenerate at the center of the Brillouin zone) and a split-off band. The energies of the heavy and light holes are given by

$$E(\mathbf{k})=E_0+(\hbar^2k^2/2m_0)[A\pm(B^2+sC^2)^{1/2}]\,,$$
$$s=(k_x^2k_y^2+k_x^2k_z^2+k_y^2k_z^2)/k^4\,, \tag{1}$$

where the plus sign is for light holes and the minus sign is for heavy holes. The parameters $A$, $B$, and $C$ determine the curvature of the bands, and hence the effective masses. The curvatures of the bands at the origin are not unique, but depend on the direction of the $\mathbf{k}$ vector.

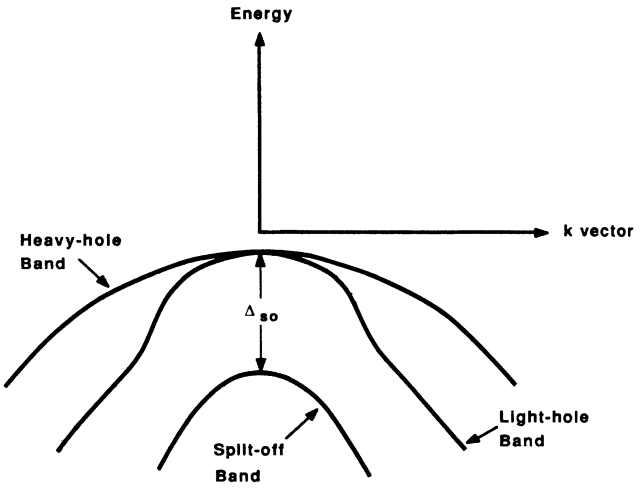


FIG. 2. Structure of the valence band at zero stress. The spin-orbit interaction splits the original $\Gamma_5$ symmetry at $k=0$ into $\Gamma_8$ and $\Gamma_7$ symmetries, separated by $\Delta_{s.o.}$.

Effective masses can still be defined by expanding the fluted energy surfaces in spherical harmonics.[26] In this spherical approximation, the average effective masses are given by

$$1/m^*_{\rm av}=(1/m_0)[A\pm(B^2+C^2/6)^{1/2}] . \quad (2)$$

The parameters $A$, $B$, and $C$ have been found from cyclotron-resonance experiments[13,14] to be $A=-4.27$, $B=-0.63$, and $|C|=4.93$ at 1.26 K. The corresponding zero-stress heavy- and light-hole masses are $m_h^*=0.47$ and $m_l^*=0.16$.

## IV. THERMAL EMISSION OF CARRIERS TO MULTIPLE BANDS

The total probability for the thermal emission of a carrier from a single defect to multiple bands is the sum of various independent emission probabilities. These bands may be degenerate, or not. For heuristic purposes the case for two distinct bands is considered first, denoted as bands 1 and 2. Since no distinction can be made whether the carrier is emitted to band 1 or to band 2, the emission processes to these bands are independent and the total emission probability per unit time becomes

$$e_0=g_1+g_2 , \quad (3)$$

where the $g_j$ are the generation rates of carriers from the defect level to band $j$. Since all the defects with the same ground state are equivalent, they will all have this same emission probability, which will lead to a single-exponential decay of the DLTS signal,

$$N(t)=N(0)e^{-e_0 t} . \quad (4)$$

The expression for $e_0$ can be obtained through detailed balance. The detailed-balance equation is

$$\sigma_1 v_1 n_1 s+\sigma_2 v_2 n_2 s=g_1 b+g_2 b , \quad (5)$$

where the subscripts 1 and 2 refer to the two different bands, $v_j$ is the thermal velocity of the carriers and $n_j$ is the number of carriers in the respective band, $s$ is the fraction of unoccupied defects, $b$ is the fraction of occupied defects, and $\sigma$ is the capture cross section, which may be different for capture from different bands. The transition processes are shown in Fig. 3.

The ratio of occupied traps to unoccupied traps is

$$b/s=\gamma\exp[-(E_T-E_F)/k_BT] , \quad (6)$$

where $E_T$ is the defect binding energy, $E_F$ is the Fermi level, and $\gamma$ is the defect degeneracy factor. For a single band the number of carriers occupying that band can be approximated as

$$n=n_i\exp[(E_F-E_i)/kT]$$
$$=N\exp[(E_{\rm band}-E_F)/k_BT] . \quad (7)$$

where $n_i$ is the intrinsic carrier concentration in the band and $E_i$ is the intrinsic Fermi level. The band effective density of states is given by

$$N=2(m^*_{\rm DOS}k_BT/2\pi\hbar^2)^{3/2} , \quad (8)$$

where $m^*_{\rm DOS}$ is the density-of-states effective mass. Equation (7) can be retained for each band separately in the multiple-band situation,

$$n_{1,2}=n_{i1,2}\exp[(E_F-E_i)/k_BT]$$
$$=N_{1,2}\exp[(E_{1,2}-E_F)/k_BT] , \quad (9)$$

where $N_{1,2}$ is the density of states defined in the same manner as for a single or degenerate band and $E_{1,2}$ is the respective band-edge energy.

Solving directly for $g_1+g_2$ gives the total emission probability,

$$e(\tau)=cT^2(\sigma_1(\tau)m_1^*(\tau)\exp\{[E_T(\tau)-E_1(\tau)]/k_BT\}$$
$$+\sigma_2(\tau)m_2^*(\tau)\exp\{[E_T(\tau)-E_2(\tau)]/k_BT\}) . \quad (10)$$

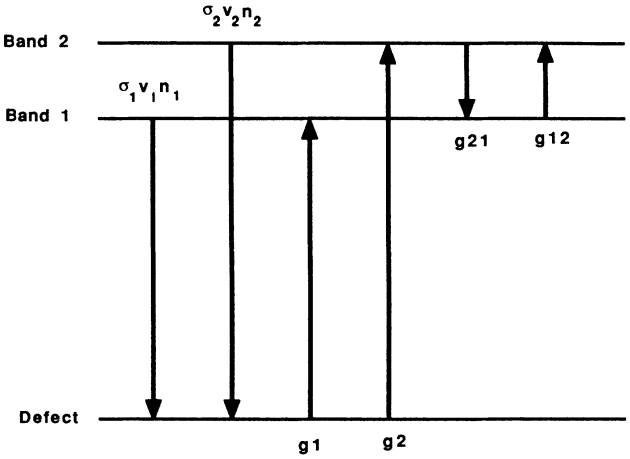


FIG. 3. Transition processes between a defect and multiple bands. The capture and thermal emission probabilities from and to two different bands are presented.

This equation is the independent-band model for emission of carriers to two bands. The stress dependence $\tau$ of the effective masses, energies, and capture cross sections have been explicitly included.

The quantities $m_1^*(\tau)$ and $m_2^*(\tau)$ are averaged effective masses arising from the mass dependencies of the thermal velocities and density of states. This average effective mass is

$$m^* = (m_{\rm DOS}^*)^{3/2}(m_{\rm th}^*)^{-1/2} , \tag{11}$$

where $m_{\rm DOS}^*$ is the density-of-states mass defined by

$$m_{\rm DOS}^* = (m_1 m_2 m_3)^{1/3} , \tag{12}$$

where the $m_i$ are the principal values of the effective-mass tensor. The thermal effective mass $m_{\rm th}^*$ is defined by the average thermal velocities $\langle v \rangle_{\rm rms}$ as

$$\begin{aligned} m_{\rm th}^* &= 3k_B T/\langle v \rangle_{\rm rms}^2 , \\ 1/m_{\rm th}^* &= \tfrac{1}{3}(1/m_1 + 1/m_2 + 1/m_3) . \end{aligned} \tag{13}$$

The emission probability in the independent-band model of Eq. (10), though a biexponential in temperature, yields a single-exponential relaxation in time, and hence a single DLTS peak. It is interesting to note, however, that the system discussed above will have a nonlinear Arrhenius plot. Although all the transients may be single exponentials, the emission rate is determined by several emission probabilities, and each probability will have a different activation energy. This presents some difficulty when attempting to determine an activation energy by plotting the emission rate as a function of $1/T$. In order to find the defect activation energy $E_T$, all parameters describing the various bands must be known accurately and used to fit the data to the above equation.

The conduction-band minima in the indirect-band-gap semiconductors represent truly independent bands with well-defined density of states and carrier effective masses. In the zero-stress limit these minima are degenerate and the carrier emission occurs to each equivalent minimum with equal probability. Under the application of uniaxial stress, the degeneracy is lifted and the minima become inequivalent. The emission process in this case is determined simply by extending Eq. (10) to include the correct number of minima and their respective energy shifts. The effective masses are not altered (to first order) by the application of stress.

The thermal emission of holes to the valence band, on the other hand, cannot be defined rigorously in terms of emission to multiple, independent bands. This is especially true for the zero- and low-stress cases. The difficulty originates from the spin-orbit interaction and the complicated structure it imposes on the top of the valence band (described in Sec. III). This structure cannot be described exactly by two independent bands at zero or low stress because the two bands mix. Furthermore, it is impossible to uniquely define an effective-mass tensor for the valence band. These features make it difficult to apply Eq. (10) to the thermal emission of carriers to the valence band. In this situation, the detailed balance equation (5) can be made more precise by replacing it with

$$\sigma_0 s \int v(E,\tau) n(E,\tau) dE = b \int g(E) dE , \tag{14}$$

where the number of carriers at energy $E$ is given by

$$n(E,\tau) = N(E,\tau)\exp[-(E-E_F)/k_B T] , \tag{15}$$

and $N(E)$ is the density of states at energy $E$. For complete generality, the stress dependence of the density of states and thermal velocity is included explicitly. The average energy- and stress-dependent thermal velocity $v(E,\tau)$ is

$$v(E,\tau) = (1/\hbar)(\mathbf{n}\cdot\nabla_{\mathbf{k}} E)_{E,\tau} ,$$

where

$$\begin{aligned} (\mathbf{n}\cdot\nabla_{\mathbf{k}} E)_{E,\tau} &= \frac{\int dS_E}{\int (\mathbf{n}\cdot\nabla_{\mathbf{k}} E)^{-1} dS_E} \\ &= \frac{\int dS_E}{4\pi^3 N(E,\tau)} , \end{aligned} \tag{16}$$

and $\mathbf{n}$ is the unit vector pointing along the direction of the $\mathbf{k}$ vector. The term $dS_E$ is a monoenergetic surface element in $\mathbf{k}$ space. The thermal emission rate is therefore

$$\begin{aligned} e_0 &= \sigma_0(\hbar\gamma)^{-1} \int (\mathbf{n}\cdot\nabla_{\mathbf{k}} E)_{E,\tau} N(E,\tau) e^{-(E_T - E)/k_B T} dE \\ &= \sigma_0(4\hbar\gamma\pi^3)^{-1} \int \left[ \int dS_E \right] e^{-(E_T - E)/k_B T} dE . \end{aligned} \tag{17}$$

Though this expression has the advantage of being rigorous, it must be evaluated numerically.

The problem can be simplified considerably by developing an independent-band model for the valence band. This model approximates the valence band as two independent bands that displace rigidly with changing stress. When this approximation is extended to the case of nonzero stress, Eq. (17) reduces to the previous equation, (10), after substitution of appropriate effective masses and energy splittings for the top of the valence band under uniaxial stress. In Sec. V the energy splittings of the valence band are described in detail and the application of the independent-band approximation is discussed.

## V. THE VALENCE BAND UNDER STRESS

### A. Energy splittings under stress

There are three deformation potentials describing the strain couplings of a $\Gamma_8$ state. These are $a$, the hydrostatic; $b$, the normal; and $d$, the shear deformation potentials. The splittings in the limit of small stresses are given by

$$\begin{aligned} [\Delta E(\tau)]^2 = (b^2/2)[&(\varepsilon_{xx} - \varepsilon_{yy})^2 + (\varepsilon_{xx} - \varepsilon_{zz})^2 + (\varepsilon_{yy} - \varepsilon_{zz})^2] \\ &+ d^2(\varepsilon_{xy}^2 + \varepsilon_{xz}^2 - \varepsilon_{yz}^2) . \end{aligned} \tag{18}$$

The deformation potentials are[11] $b = -2.1$ eV and $d = -5.1$ eV at 77 K. The splittings described by Eq. (18) are only valid in the limit of small stresses such that the valence-band splitting is negligible compared to the spin-orbit splitting $\Delta_{\rm s.o.}$. For stresses greater than 0.1 GPa,

however, the coupling of the top of the valence band with the split-off band is strong enough to produce significant corrections to the shifts described in Eq. (18). The coupling of the top of the valence band to the split-off band under uniaxial deformation can be calculated directly for all stress directions and magnitudes by extending the stress Hamiltonian of Pikus and Bir[27] to include the split-off band. This Hamiltonian represents the valence bands according to the $j=\frac{3}{2}$ and $\frac{1}{2}$ angular momenta. The eigenvalues of the full $6\times6$ Hamiltonian matrix reduce to three values with double (Kramers) degeneracy, because stress does not break time-reversal symmetry. For stresses along either the $\langle 100\rangle$ or $\langle 111\rangle$ directions, the $z$ component of the angular-momentum quantum numbers $m_J$ remain good quantum numbers, and if the stress direction is taken as the quantization axis, then there are no matrix elements of the stress Hamiltonian between states with $m_J$ and $-m_J$. The Hamiltonian for [001] stress reduces to a $1\times1$ matrix for the $m_J=\pm3/2$ and a $2\times2$ matrix for the $m_J=\pm\frac{1}{2}$. The $2\times2$ matrix has the following eigenvalues:

$$E=\frac{E_{100}}{4}-\frac{\Delta_{\text{s.o.}}}{2}\pm\frac{\Delta_{\text{s.o.}}}{2}\left[1+\tfrac{9}{4}\left[\frac{E_{100}}{\Delta_{\text{s.o.}}}\right]^2+\left[\frac{E_{100}}{\Delta_{\text{s.o.}}}\right]\right]^{1/2}, \tag{19}$$

where $E_{100}=2b(s_{11}-s_{12})T$. For the case of stress in the [111] direction, the quantization axis can be rotated to coincide with the stress axis to obtain similar eigenvalues. For the case of arbitrary stress direction the $m_J$ are no longer good quantum numbers and the Hamiltonian reduces to a $3\times3$ matrix which yields three eigenvalues. The energy shifts for stress parallel to [100] are shown in Fig. 4 compared to the shifts described by Eq. (18) in the absence of coupling to the split-off band. Under [100] compression the $\Gamma_8$ degenerate valence band splits into $X_6$ and $X_7$ Kramers-doublet representations with the $X_7$ band moving into the band gap. This $X_7$ band couples with the $X_7$ split-off band, producing nonlinear shifts for the top of the valence band. The interaction under 1 GPa produces nearly a 50% correction to the value predicted by Eq. (18). The angular dependence of the energy shifts for 1 GPa is shown in Fig. 5 in comparison with the splittings of the $\Gamma_5$ state in the absence of spin-orbit splitting. One of the remarkable features of the valence band under stress is the fact that the energy shifts are isotropic within 10%.

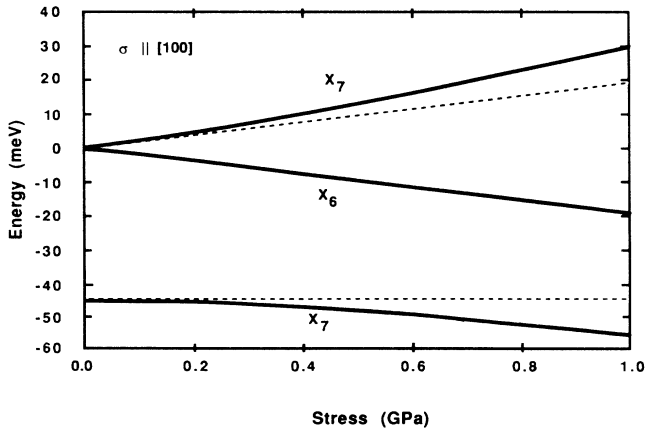


FIG. 4. Energy splitting and shifts of the top of the valence band and the split-off band for compressive stress along [100]. The parameters used in Eq. (19) are $b=-2.1$ eV and $\Delta_{\text{s.o.}}=44$ meV.

The energy splittings defined by Eq. (18) are valid only for the valence-band extrema at the $\Gamma$ point for zero **k** vector. Points on the dispersion curve for finite **k** vector will shift by different amounts, depending on the magnitude as well as direction of the **k** vector. In other words, the bands are not rigidly displaced in energy, but are warped by the application of stress. Yet, the energy splittings of Eq. (18) are convenient to use in the independent-band approximation as the energies by which two independent bands are rigidly displaced. The effect of the additional warping under stress of the originally fluted energy surfaces must therefore be included as changes in the effective masses describing the density of states and the thermal velocities. The appropriate effective masses which enter the independent-band approximation are discussed next.

### B. Effective masses under stress

The effective mass of a band extremum is inversely proportional to the curvature of the electron energy as a function of the **k** vector. Bands described by spherical energy surfaces have a unique effective mass, while bands described by elliptical or spheroidal energy surfaces can

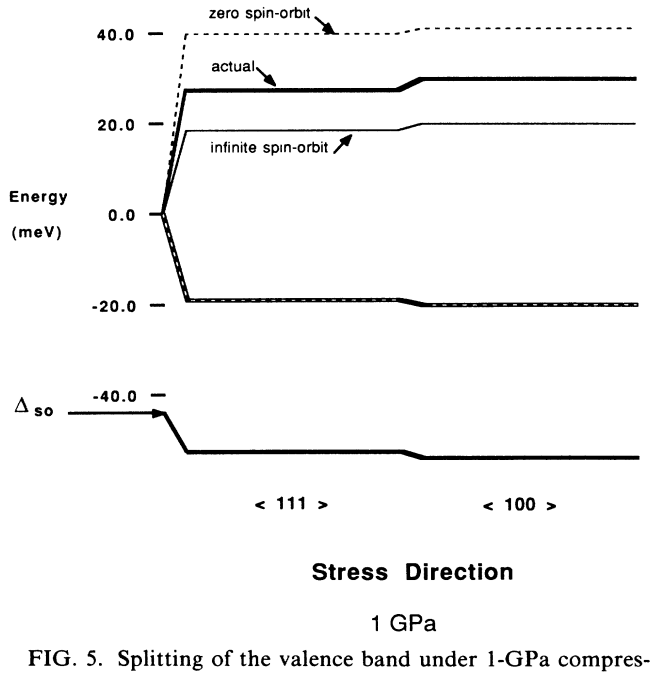


FIG. 5. Splitting of the valence band under 1-GPa compressive uniaxial stress. The dotted line is for the case of no spin-orbit interaction, the thin solid line is for the case of infinite spin-orbit coupling, and the bold solid line is the actual valence-band shift under 1 GPa.

be described uniquely by effective-mass tensors. The density-of-states effective mass $m^*_{\rm DOS}$ is defined in Eq. (12) as the cube root of the product of the principal values of the mass tensor. The energy surfaces of the valence band at zero stress, however, are not elliptical or spheroidal, but are described by fluted or warped spheres. This makes it impossible to uniquely define an effective-mass tensor, as stated before.

The structure of the valence band becomes much simpler for high stresses applied along the $\langle 100\rangle$ or $\langle 111\rangle$ directions. For large stresses in these directions (strain energy $\gg k_B T$), the energy surfaces are described by prolate and oblate spheroids which do have well-defined effective-mass tensors. The principal values of the effective masses for these stress directions[8] are given in Table I where $N^2=3(B^2+C^2)$.

The function

$$Z(x)=\tfrac{1}{2}[1+(1-9x)(1-2x+9x^2)^{-1/2}] \tag{20}$$

describes the effect of coupling to the split-off band on the principal values of the effective-mass tensor, where the quantity $x=\Delta E(\tau)/\Delta_{\rm s.o.}$.

The function $Z(x)=1$ in the absence of coupling to the split-off band. For 1 GPa, the value for silicon is $Z(x=0.4)=-0.6$, which dramatically alters the principal values of the effective-mass tensor, and has important consequences in ESR.[13] The density-of-states mass, however, remains surprisingly unaffected ($<5\%$ at 1 GPa) and therefore this extra mixing of the effective mass can be neglected in stressed DLTS. It is interesting to point out that these high-stress effective masses have the property that the average thermal inverse effective mass is exactly

$$1/m^*_{\rm th}=\tfrac{1}{3}\sum_i (1/m_i)=A\ , \tag{21}$$

independent of the strength of the coupling to the split-off band.[8] The valence band under large stress is accurately described by two rigidly displacing, independent bands with well-defined effective masses; no approximations are required.

The situation for small stress (strain energy $\ll k_B T$) is substantially more complicated than the case of large stress because of the strong mixing of the originally degenerate bands. Again, as in the zero-stress case, there is no unique method to define an effective density-of-states mass. Two methods are described next to define average stress-dependent density-of-states effective masses. The first method defines the effective masses through the curvature of the energy dispersion. The second method defines the valence band as two rigidly displacing parabolic bands and finds the appropriate density-of-states effective masses for these bands. Both of these methods begin with the Bir-Pikus strain Hamiltonian describing the energy shifts under stress of the electron-energy dispersion curves.

TABLE I. Principal values of effective masses for listed stress directions.

| $\langle 100\rangle$ | $\langle 111\rangle$ |
|---|---|
| $m_{1/2,\parallel}=1/[A+BZ(x)]$ | $m_{1/2,\parallel}=1/[A+\frac{1}{3}NZ(x)]$ |
| $m_{1/2,\perp}=1/[A-\frac{1}{2}BZ(x)]$ | $m_{1/2,\perp}=1/[A-\frac{1}{6}NZ(x)]$ |
| $m_{3/2,\parallel}=1/(A-B)=0.28$ | $m_{3/2,\parallel}=1/(A-\frac{1}{3}N)=0.75$ |
| $m_{3/2,\perp}=1/(A+\frac{1}{2}B)=0.22$ | $m_{3/2,\perp}=1/(A+\frac{1}{6}N)=0.18$ |

In the absence of coupling to the split-off band, the hole Hamiltonian including stress and $\mathbf{k}$ vector is[27]

$$\begin{aligned}
&E(\mathbf{k})=Ak^2+a\Delta\pm(E_{k^2}+E_{\varepsilon k}+E_{\varepsilon^2})^{1/2}\ ,\\
&E_{k^2}=B^2k^4+C^2(k_x^2k_y^2+k_x^2k_z^2+k_y^2k_z^2)\ ,\\
&E_{\varepsilon^2}=\tfrac{1}{2}b^2[(\varepsilon_{xx}-\varepsilon_{yy})^2+(\varepsilon_{xx}-\varepsilon_{zz})^2+(\varepsilon_{yy}-\varepsilon_{zz})^2]\\
&\qquad +d^2(\varepsilon_{xy}^2+\varepsilon_{xz}^2+\varepsilon_{yz}^2)\ ,\\
&E_{\varepsilon k}=Bb[3(k_x^2\varepsilon_{xx}+k_y^2\varepsilon_{yy}+k_z^2\varepsilon_{zz})-k^2\Delta]\\
&\qquad +2Dd(k_xk_y\varepsilon_{xy}+k_xk_z\varepsilon_{xz}+k_yk_z\varepsilon_{yz})\ ,
\end{aligned} \tag{22}$$

where $\Delta=(s_{11}+2s_{12})\mathcal{T}$ is the dilatation ($\mathcal{T}$ is the stress and is negative for compressive strain). The spherical approximation of the valence band[26] can be extended to include stress by deriving the appropriate irreducible-spherical-tensor operator that represents the strain field caused by applied uniaxial stress.[28] Stress-dependent effective masses can also be obtained through numerical calculations by finding the curvature in the two branches[29] of Eq. (22). Qualitatively similar results are obtained by replacing $B$, $C$, and $D$, respectively, in the above equation by

$$\begin{aligned}
&B'=(B^2+\tfrac{1}{6}C^2)^{1/2}\ ,\\
&C'=0\ ,\\
&D'=\sqrt{3}B'\ .
\end{aligned} \tag{23}$$

The new Hamiltonian gives (by definition) the correct effective masses of zero stress. For finite strain the effective masses are found by calculating the curvature of the two branches of Eq. (22) for directions parallel and perpendicular to the applied stress direction and applying Eq. (12). Thermal averages are taken by weighting the curvature with the Boltzmann factor. The effective masses are therefore functions of both stress and temperature. The results for the density-of-states effective masses at 77 and 20 K are given in Fig. 6. The light and heavy holes mix quickly with increasing stress, and saturate to constant values defined by Eq. (21) for high stress. The mixing rate is faster for lower temperature because the effective mass is dominated by the curvature at smaller $\mathbf{k}$ vector and the high-stress limit is approached more quickly.

### *1. Density of states*

The second approach for defining the stress-dependent effective masses (in the independent-band model) obtains the stress and energy-dependent density of states of the valence band. This density of states is used with the energies given by Eq. (18) to fit the effective masses for the rigid, independent bands. The density of states of a band is defined by the electron-energy dispersion equation

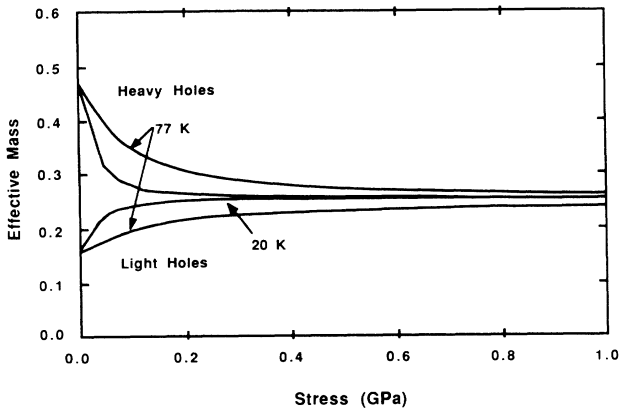


FIG. 6. Mixing of the effective masses calculated from the spherical approximation under compressive stress along [100].

$E(\mathbf{k},\tau)$ through the integral

$$N(E,\tau)=\int \delta(E-E(\mathbf{k},\tau))d\mathbf{k} \ . \tag{24}$$

This integration was carried out numerically for the case of compressive stress applied along the [100] and [111] axes. By symmetry, for [100] stress, only $\frac{1}{16}$ of the Brillouin zone is considered. For [111] stress only $\frac{1}{12}$ of the Brillouin zone is sampled. Furthermore, it is only necessary to consider the density of states within several $k_BT$ of the band extremum, which limits the magnitudes of the $\mathbf{k}$ vector to only $\frac{1}{20}$ of the value of at the Brillouin-zone boundary. Therefore, the volume of $\mathbf{k}$ space sampled in the integration was approximately $\frac{1}{300}$ of the volume of the Brillouin zone. Within this volume, 50 000 points were sampled. The results of the integration for [100] stress are shown as the data points in Figs. 7(a)–7(c) for $\tau=0.0$, 0.3, and 0.6 GPA, respectively. Results for [111]-oriented stress are quantitatively similar. Coupling to the split-off band was neglected in this effective-mass analysis. The solid curves are the result of the independent-band model. This model predicts density of states that vary as the square root of energy, with a multiplicative prefactor that depends on the effective mass of the respective band raised to the $\frac{3}{2}$ power [from Eq. (8)]. The model fits the numerical data well for zero stress, but there are deviations from the independent-band model for finite stress. The deviations occur within the region of energy in which the two bands are strongly mixed. This interaction modifies the curvature of the energy dispersion relation through avoided crossings, which directly affects the density of states.

The dependence of the thermal-emission probability on the density of states is weighted exponentially towards the band edge. Therefore, to compare the results of Fig. 6 with the results of the numerical calculation of $N(E,\tau)$, it is convenient to define a thermal density of states by

$$\mathcal{N}=\int N(E,\tau)\exp(-E/k_BT)dE/N(E,0) \ . \tag{25}$$

The inverse of this quantity as a function of stress is plotted in Fig. 8 for the numerical calculations. In the independent-band model, Eq. (25) is equivalent to

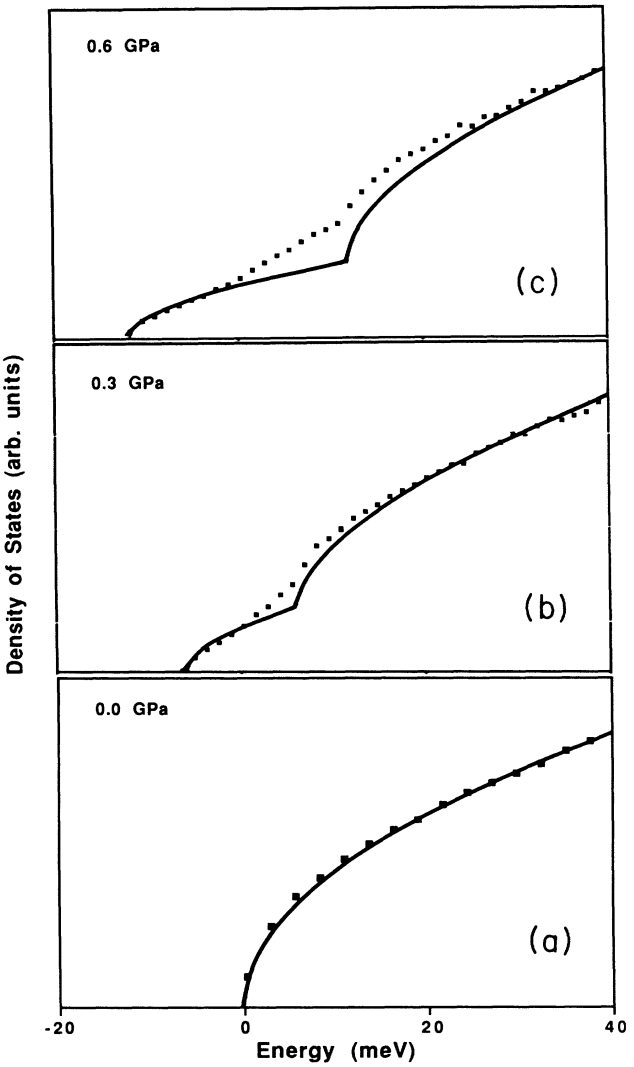


FIG. 7. Density of states of the valence band for (a) O GPa, (b) 0.3 GPa, and (c) 0.6 GPa of compressive uniaxial stress applied along [100]. The best fit of two independent parabolic bands is included as the solid line.

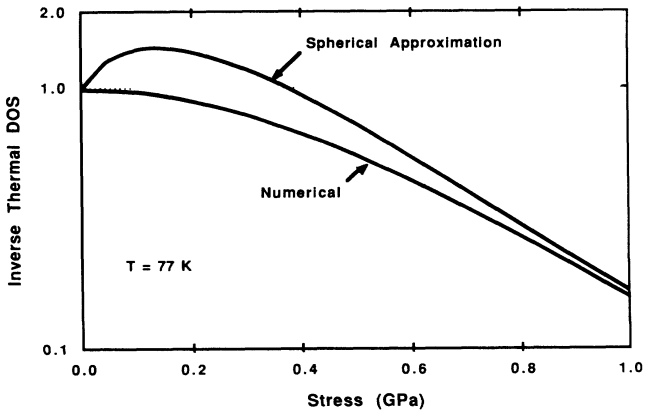


FIG. 8. Inverse thermal density of states defined by Eq. (25) as a function of compressive stress at $T=77$ K. The curve labeled Spherical Approximation uses the effective masses from Fig. 6. The curve labeled Numerical is the exact result using the accurate density of states from Eq. (24). Compare these curves with the Fe-Al data in Fig. 15.

$$\mathcal{N}=\frac{[m_l(\tau)]^{3/2}\exp(E_\varepsilon/k_BT)+[m_h(\tau)]^{3/2}\exp(-E_\varepsilon/k_BT)}{[m_l(0)]^{3/2}+[m_h(0)]^{3/2}}, \tag{26}$$

where $m_l(\tau)$ and $m_h(\tau)$ are the stress-dependent effective light- and heavy-hole masses, and $E_\varepsilon$ is the energy shift of the respective band edge defined in Eq. (18). The result of Eq. (26), using the effective masses from the spherical approximation, is compared in Fig. 8 to the exact numerical result from Eq. (25). This function is proportional to the fractional change in the emission time from a defect that is insensitive to stress. The result of the spherical approximation clearly disagrees with the exact numerical calculation for low stresses. The spherical approximation would predict an increase of the emission time for small stresses. For low stresses the emission would still be predominantly to the heavy-hole band, which is moving away from the defect energy (although the thermal emission is weighted by a Boltzmann factor), because the heavy-hole band has the larger effective density of states. This produces the initial increase in the emission time constant. With increasing stress, however, the Boltzmann factor increasingly favors emission to the light-hole band, which is approaching the defect energy, and therefore the time constant eventually decreases. Under the higher stresses, the values of the spherical approximation approach the exact numerical values. This demonstrates that the spherical approximation does, in fact, give the correct density of states in the limit of zero stress, as well as the correct effective mass for the light hole in the limit of large stress. However, the predicted partitioning of the density of states between the two bands by the spherical approximation is incorrect. The error has arisen from the (incorrect) use of the effective masses from the spherical approximation with the band-edge splittings [Eq. (18)]. The energies and effective masses cannot be defined separately. Once one of these quantities is defined, the other quantity is completely determined. The energy splittings of the band edges are well established, and therefore it is convenient to retain these energies and then find the appropriate effective masses for the density of states. The need to redefine the effective masses of holes in semiconductors for a given application is a common problem. Because there is no unique way to define the hole masses, each application must use values suited to its own peculiarities. For instance, hole effective masses measured in cyclotron resonance have been shown to be a function of the Fermi level.[30] The correct effective DOS masses as a function of stress for thermal emission can be derived by fitting the masses in Eq. (26) to the numerical results of Eq. (25). The resulting DOS effective-mass values are shown in Fig. 9 for 77 K. At zero stress the two masses are nearly equal, in strong contradiction to the spherical approximation, yet the total density of states is the same for both models. At high stresses, the light-hole effective mass approaches the asymptote $1/A$ correctly described by Eq. (21).

The near equality of the DOS light- and heavy-hole effective masses at low stress has the important consequence that the center of gravity of the splitting valence bands is approximately conserved as stress is increased. This fact is reflected by the zero-slope asymptote of the thermal density of states in Fig. 8 for zero stress. This would not be the case if the masses from the spherical approximation were used; in that case the center of gravity would shift away from the band edge. Shifts in the center of gravity of electronic states are caused by the trace (or hydrostatic component) of the strain tensor, which has already been included by the term $a\Delta$ in Eq. (22).

### 2. *Thermal effective masses*

The effective mass that is used to define the effective density of states has a different origin than the effective mass that describes the thermal velocity of carriers in the band. Though the thermal and density-of-states masses are certainly related through the curvature of the energy dispersion, it remains to establish the connection between the two masses and find the combined effective mass of Eq. (11). This is done numerically by integrating Eq. (16) over **k** space in analogous fashion to the evaluation leading to the density of states $N(E)$. The calculated average velocity as a function of energy is plotted in Figs. 10(a)–10(c) for 0.0, 0.3, and 0.6 GPa of compressive uniaxial stress oriented along the [100] direction. The best fit from the independent-band model is included as the solid line. The independent-band model clearly overestimates the velocity in the region near the strong mixing of the two bands, just as the model underestimates the density of states in Fig. 7 in the same energy region. This is a direct consequence of the interaction of the two bands which results in avoided crossing (from symmetry considerations). The avoided crossing changes the curvatures and slopes of the bands near the crossing point and therefore alters the density of states and thermal veloci-

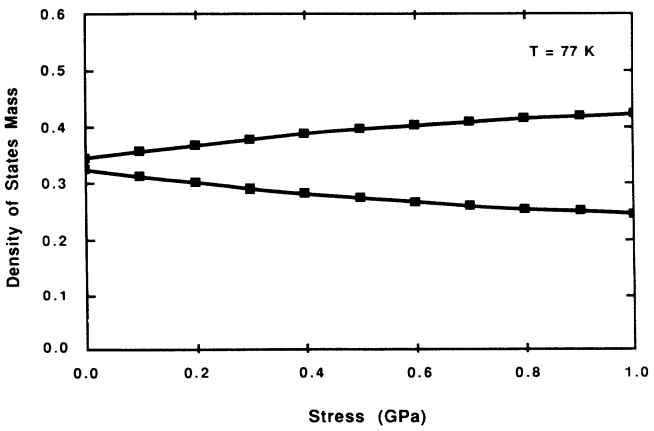


FIG. 9. Density-of-states effective masses as functions of stress derived from the exact thermal density of states in Fig. 8 using Eq. (26).

ties. The independent-band model therefore has difficulty modeling the density of states and the energy-dependent velocities separately near the crossover between the light- and heavy-hole bands for moderate stresses.

### 3. *Thermal emission probability*

Thermal emission probabilities do not depend on the density of states and thermal velocities separately, but depend on the product of these properties [see Eq. (5)]. This product is presented in Fig. 11 for the three stresses of Figs. 7 and 10. Both the density of states and the velocity depend on the square root of the energy, so the independent-band model predicts a linear dependence on energy for the product of the two values. The best fit from the independent-band model is included as the solid curves. The independent-band model gives an excellent fit to the numerical calculations for all values of stress,

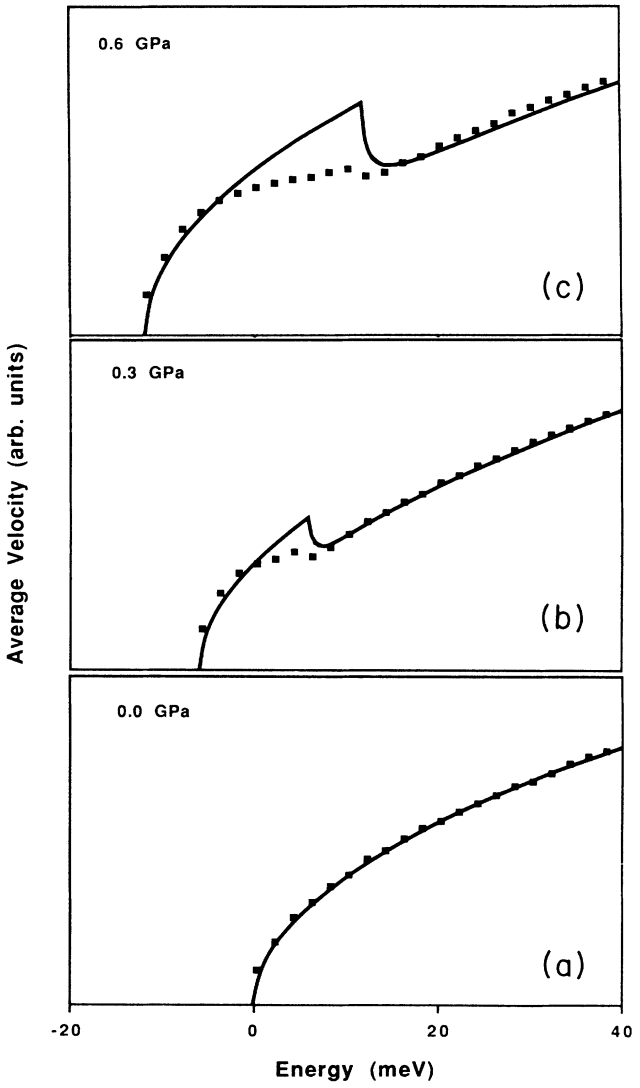


FIG. 10. Average energy-dependent velocity for (a) zero stress, (b) 0.3 GPa, and (c) 0.6 GPa. The solid curves are the best fit from the independent-band model.

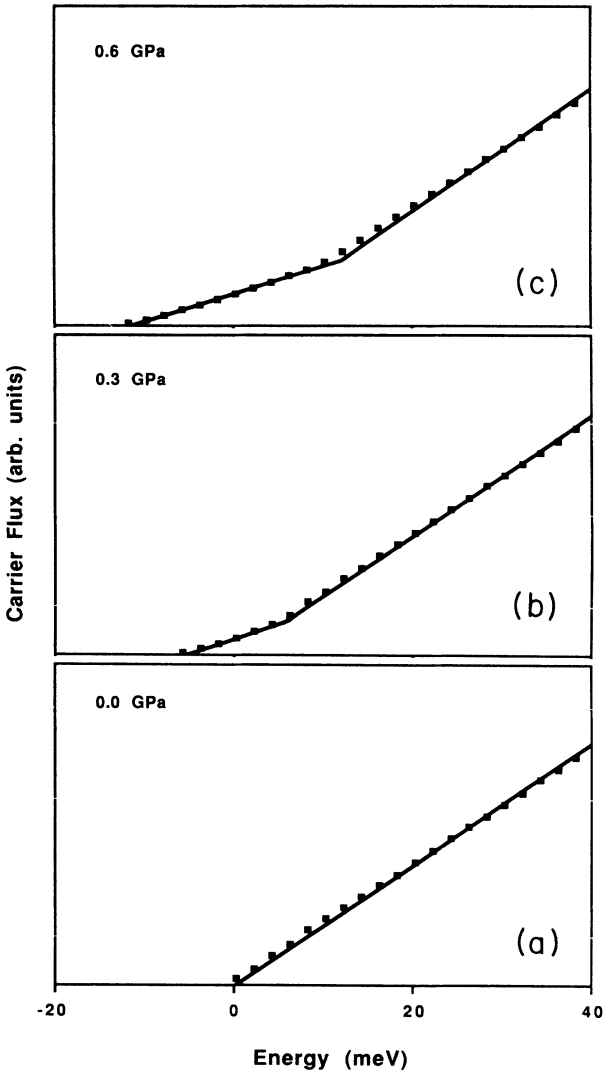


FIG. 11. Product of Figs. 6 and 9 for (a) zero stress, (b) 0.3 GPa, and (c) 0.6 GPa. This product is directly proportional to the probability for the emission of a carrier to the given energy. The independent-band model gives a good fit for all stresses.

even in the energy region in which there is strong mixing of the two bands. This is because the thermal emission is insensitive to the dynamics of the holes (and hence the avoided crossing) and only samples the phase space available to emission through the term ( $\int dS_E$ ) in Eq. (17).

To find the appropriate combined effective mass of Eq. (11), the full thermal-emission-rate equation (17) is evaluated numerically and compared to the normalized thermal emission rate based on the independent-band model,

$$\frac{e_0(\tau)}{e_0(0)}=\frac{m_l(\tau)\exp(E_\varepsilon/k_BT)+m_h(\tau)\exp(-E_\varepsilon/k_BT)}{m_l(0)+m_h(0)} . \tag{27}$$

The resulting values for the combined effective masses are shown in Fig. 12. From the DOS and combined effective masses, the thermal effective mass is derived from Eq. (11). All three effective masses for the light holes are

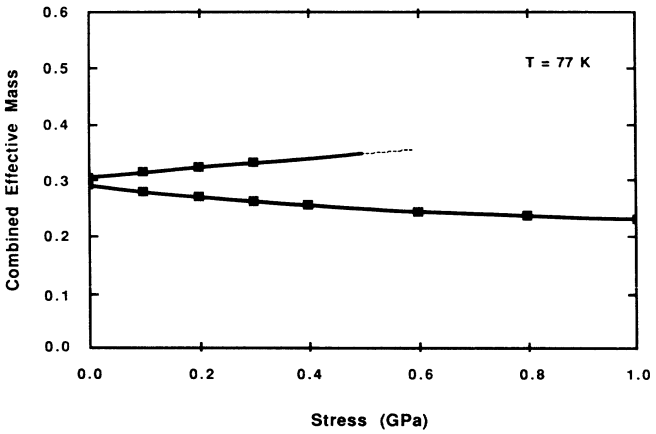


FIG. 12. Combined effective mass fitted to the numerical results of Fig. 11 based on the independent-band model of Eq. (27).

given in Fig. 13 for compressive uniaxial stress oriented along the [100] direction at $T=77$ K. The heavy-hole masses are approximately given by $m_h^*(\tau)=2m_l^*(0)-m_l^*(\tau)$.

In this section we have presented the energy shifts and the effective masses appropriate for the independent-band model describing the heavy- and light-hole valence bands under uniaxial stress. The understanding of how these parameters vary with stress is essential to derive the energy shifts of a defect under stress from the independent-band model of Eq. (10). To test the completeness of this understanding of the valence band, it is useful to observe the DLTS spectrum of a defect which is insensitive to stress. This defect level can act as a reference level from which the properties of the valence band under stress can be measured. Iron-aluminum pairs in $p$-type Si are chosen as stress-insensitive reference levels. Using the Fe-Al level as a reference, the validity of the independent-band model is tested by applying the stress-dependent effective mass shown in Fig. 12.

## VI. IRON-ALUMINUM PAIRS AS REFERENCE LEVELS

Representative examples of stress data for the Fe-Al-1 and Fe-Al-2 defects are shown in Fig. 14 for ⟨100⟩ stress and for a constant emission rate. The large shifts in temperature under stress are predominantly from the splitting of the top of the valence band. The shifts in the temperature of the defect peak positions for increasing stress are shown in Figs. 15(a)–15(d) for the two defects under [100] and [111] stresses. The solid lines are the best fit of the data to Eq. (10) using the combined effective masses of Fig. 12. The only free parameter is the shift of the defect energy under stress, which in all cases is small compared to the shift of the valence-band edge. The data fit the theory well in all cases. It is important to note that there is no evidence of an increase in the peak temperature under small stresses as is incorrectly predicted by the spherical approximation. The final shear anisotropy of the Fe-Al defects is presented in Fig. 16. There is a consistent anisotropy of 5 meV/GPa for both defects which may reflect a relative error between the accepted values of $b$ and $d$, or may originate with the defect. The baseline is shifted for the Fe-Al-1 defect relative to the Fe-Al-2 defect. It is not clear whether this baseline shift is a property of the defect, or whether it is an artifact of the fitting analysis. One possibility is that it may be related to the increase of the effective masses with increasing temperature.[31,32] This may cause a systematic error in the absolute emission rates of the defects, but should not affect the anisotropy.

## VII. CONCLUSIONS

The application of uniaxial stress to probe the structure of deep-level defects in semiconductors has had strong success when applied to defects in $n$-type silicon. Though the applied stress splits the originally degenerate conduction-band minima, the bands shift rigidly under

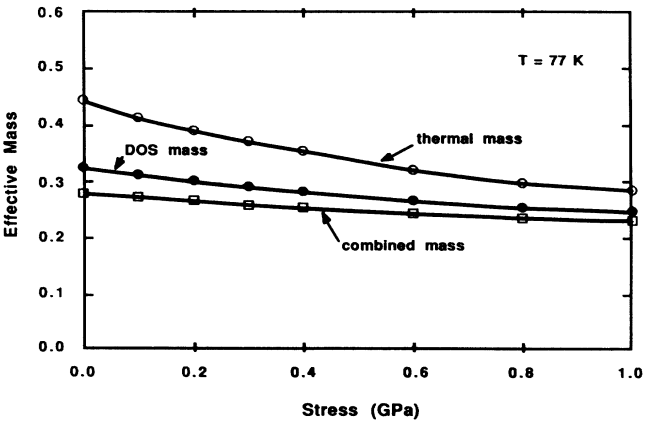


FIG. 13. Density-of-states, thermal, and combined effective masses for the light-hole band as functions of stress. The corresponding heavy-hole masses are given roughly by $m_h^*(\tau)=2m_l^*(0)-m_l^*(\tau)$.

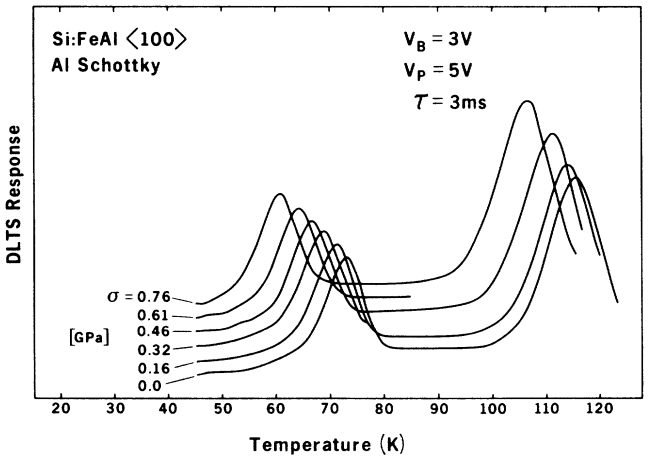


FIG. 14. Typical DLTS spectrum of the Fe-Al defect pairs for increasing stress. The data are taken with a constant rate window. The low- and high-temperature peaks are from Fe-Al-2 and Fe-Al-1, respectively.

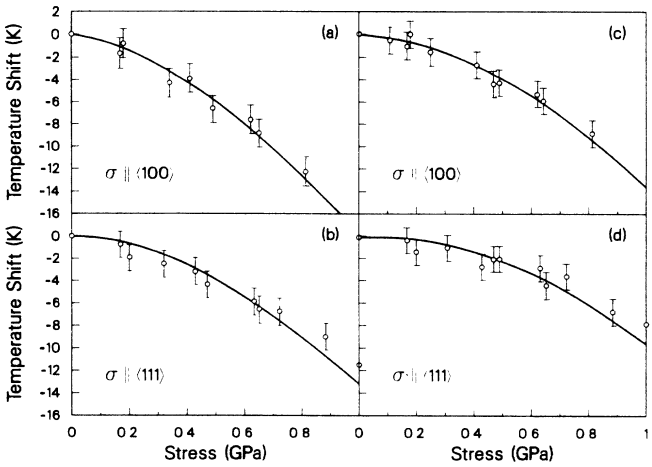


FIG. 15. Change in the temperature at which the DLTS peak reaches a maximum with increasing stress for a constant emission rate for (a) Fe-Al-2 under [100] stress, (b) Fe-Al-2 under [111] stress, (c) Fe-Al-1 under [100] stress, and (d) Fe-Al-1 under [111] stress.

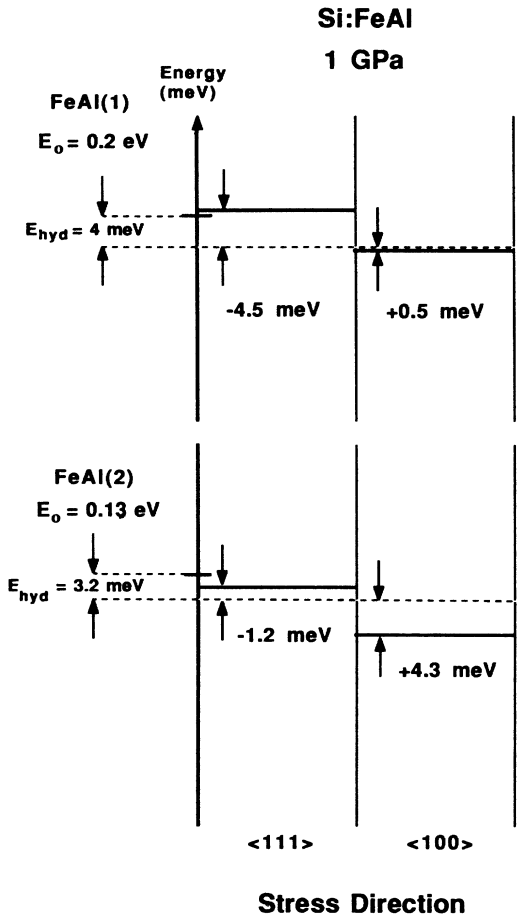


FIG. 16. Shear energy dependence of the Fe-Al-1 and Fe-Al-2 defects fitted from the independent-band model and the data of Fig. 15.

stress. The deformation potentials are accurately known, and there is no mixing of the effective masses to first order in the stress. Therefore, the conduction band presents no fundamental complication to the analysis of defect shifts and splittings. The treatment of the valence band in *p*-type silicon under uniaxial stress, on the other hand, presents formidable problems to the analysis of energy shifts of deep hole traps. Although the valence-band deformation potentials are known accurately, the fluted energy surfaces make it impossible to define unique effective masses. The effective masses play a vital role in determining the probability for the thermal emission of carriers to the band edge. Without an accurate knowledge of these effective masses, it is impossible to accurately derive the energy shifts of a hole trap under uniaxial stress from thermal emission experiments.

In this paper we have undertaken to consider all aspects of the valence band under uniaxial stress which enter into the emission of carriers from a deep level. We found that an independent-band model can accurately describe the effects of stress on the thermal emission rate. Two components enter into an independent-band model: the energy shifts and the effective masses. These quantities cannot be defined independently. Once one is defined, the other quantity must be consistent with it. For the valence band in silicon, the energy shifts are well known, and therefore we choose the standard values for the deformation potentials $b$ and $d$ to define the energy shifts of the rigid bands. The effective masses which must be used with these deformation potentials are set by the density of states of the Bir-Pikus Hamiltonian. The spherical approximation partitions the density of states of the valence band into two independent parabolic bands, one with large curvature and one with small curvature. This approximation is sufficient for use in zero-stress thermal emission rates because it does give the correct effective density of states. It is also appropriate for use in the effective-mass approximation for defects with shallow energy levels because only the curvature of the bands at the $\Gamma$ point enter into the theory, but it fails in the partitioning of the density of states between the two independent bands. Through numerical calculations it is found that the density of states is divided roughly equally between the two rigidly displacing bands. This partitioning conserves the center of gravity of the split bands. The analysis described in this paper for silicon can be easily generalized to study the stress dependence of hole traps in any *p*-type semiconductor with the diamond or zinc-blende structures.

## ACKNOWLEDGMENTS

We gratefully acknowledge useful discussions with W. Walukiewicz, L. M. Falicov, and M. Cohen. This work was supported by the Director, Office of Energy Research, Office of Basic Energy Sciences, Materials Science Division, of the U.S. Department of Energy under Contract No. DE-AC03-76SF00098.

*Present address: AT&T Bell Labs, Holmdel, NJ 07733.

[1]E. E. Haller, M. R. Heuschen, and P. L. Richards, Appl. Phys. Lett. **34**, 495 (1979).

[2]J. M. Meese, J. W. Farmer, and C. D. Lamp, Phys. Rev. Lett. **51**, 1286 (1983).

[3]J. L. Benton, K. M. Lee, P. E. Freeland, and L. C. Kimerling, in *Thirteenth International Conference on Defects in Semiconductors, Coronado, California, 1984,* edited by L. C. Kimerling and J. M. Pursey (Metallurgical Society of AIME, Warrendale, 1985), p. 647.

[4]C. T. Sah, L. Forbes, L. L. Rosier, and A. F. Tasch, Solid State Electron. **13**, 759 (1970).

[5]D. V. Lang, J. Appl. Phys. **45**, 3023 (1974),

[6]G. L. Miller, D. V. Lang, and L. C. Kimerling, *Annual Review of Material Science* (Annual Reviews, Palo Alto, 1977), pp. 337–448.

[7]D. V. Lang, *Thermally Stimulated Relaxation in Solids,* edited by P. Braunlich (Springer-Verlag, Berlin, 1979), pp. 109–134.

[8]H. Hasegawa, Phys. Rev. **129**, 1029 (1963).

[9]D. E. Aspnes and M. Cardona, Phys. Rev. B **17**, 726 (1978).

[10]G. Dresselhaus, A. F. Kip, and C. Kittel, Phys. Rev. **98**, 368 (1955).

[11]J.-C. Merle, M. Capizzi, P. Fiorini, and A. Frova, Phys. Rev. B **12**, 4821 (1978).

[12]L. D. Laude, F. H. Pollak, and M. Cardona, Phys. Rev. B **3**, 2623 (1971).

[13]J. C. Hensel and G. Feher, Phys. Rev. **129**, 1041 (1963).

[14]I. Balslev and P. Lawaetz, Phys. Lett. **19**, 6 (1965).

[15]G. W. Ludwig and H. H. Woodbury, in *Solid State Physics,* edited by F. Seitz and D. Turnbull (Academic, New York, 1962), Vol. 13, p. 223.

[16]J. J. van Kooten, G. A. Weller, and C. A. J. Ammerlan, Phys. Rev. B **30**, 4564 (1984).

[17]W. Gehlhof and K. H. Segsa, Phys. Status Solidi B **115**, 443 (1983).

[18]K. Wünstel and P. Wagner, Appl. Phys. A **27**, 207 (1982).

[19]L. C. Kimerling and J. L. Benton, Physica (Utrecht) **116B**, 297 (1983).

[20]Alain Chantre and D. Bois, Phys. Rev. B **31**, 7979 (1985).

[21]J. Trombetta, D. D. Nolte, E. E. Haller, and G. D. Watkins (unpublished).

[22]D. D. Nolte, Ph.D. thesis, University of Califronia, Berkeley, 1988 (unpublished).

[23]D. D. Nolte, W. Walukiewicz, and E. E. Haller, Bull. Am. Phys. Soc. **32**, 515 (1987).

[24]K. Wünstel, O. Kumagai, P. Wagner, and W. Jantsch, Appl. Phys. A **27**, 251 (1982).

[25]J. Weber (private communication).

[26]N. O. Lipari and A. Baldereschi, Phys. Rev. Lett. **25**, 1660 (1970).

[27]G. E. Pikus and G. L. Bir, Fiz. Tverd. Tela (Leningrad) **1**, 1642(1959) [Sov. Phys.—Solid State **1**, 1502 (1960)].

[28]J. Broeckx and J. Vinnik, Phys. Rev. B **35**, 6165 (1987).

[29]S. M. Kelso, Phys. Rev. B **25**, 1116 (1982).

[30]N. Garcia and L. M. Falicov, Solid State Commun. **16**, 891 (1975).

[31]H. D. Barber, Solid State Electron. **10**, 1039 (1967).

[32]F. L. Madarasz, J. E. Lang, and P. M. Hemeger, J. Appl. Phys. **52**, 4646 (1981).